

Histogram of Gradient Orientations of Signal Plots applied to P300 Detection

Rodrigo Ramele^{1,*}, Ana Julia Villar¹ and Juan Miguel Santos¹

¹*Centro de Inteligencia Computacional, Computer Engineering Department, Instituto Tecnológico de Buenos Aires (ITBA), Buenos Aires, Argentina*

Correspondence*:

Rodrigo Ramele, C1437FBH Lavarden 315, Ciudad Autónoma de Buenos Aires, Argentina
rramele@itba.edu.ar

2 ABSTRACT

3 Word Count: 5552

4 The analysis of Electroencephalographic (EEG) signals is of ulterior importance to aid in the
5 diagnosis of mental disease and to increase our understanding of the brain. Traditionally, clinical
6 EEG has been analyzed in terms of temporal waveforms, looking at rhythms in spontaneous
7 activity, subjectively identifying troughs and peaks in Event-Related Potentials (ERP), or by
8 studying graphoelements in pathological sleep stages. Additionally, the discipline of Brain
9 Computer Interfaces requires new methods to decode patterns from non-invasive EEG signals.
10 This field is developing alternative communication pathways to transmit volitional information
11 from the Central Nervous System. The technology could potentially enhance the quality of life
12 of patients affected by neurodegenerative disorders and other mental illness. This work mimics
13 what electroencephalographers have been doing clinically, visually inspecting and categorizing
14 phenomena within the EEG by the extraction of features from images of signal plots. These
15 features are constructed based on the calculation of histograms of oriented gradients from pixels
16 around the signal plot. It aims to provide a new objective framework to analyze, characterize and
17 classify EEG signal waveforms. The feasibility of the method is outlined by detecting the P300, an
18 ERP elicited by the oddball paradigm of rare events, and implementing an offline P300-based BCI
19 Speller. The validity of the proposal is shown by offline processing a public dataset of Amyotrophic
20 Lateral Sclerosis (ALS) patients and an own dataset of healthy subjects.

21 **Keywords:** **electroencephalography, histogram of gradient orientations, brain-computer interfaces, P300, SIFT, amyotrophic lateral**
22 **sclerosis, naive-bayes near neighbours, waveforms**

1 INTRODUCTION

23 Although recent advances in neuroimaging techniques, particularly radio-nuclear and radiological
24 scanning methods (Schomer and Silva, 2010), have diminished the prospects of the traditional
25 Electroencephalography (EEG), the advent and development of digitized devices has impelled for a
26 revamping of this hundred years old technology. Their versatility, ease of use, temporal resolution, ease of
27 development and production, and its proliferation as consumer devices, are pushing EEG to become the
28 de-facto non invasive portable or ambulatory method to access and harness brain information (De Vos and
29 Debener, 2014).

30 A key contribution to this expansion has been the field of Brain Computer Interfaces (BCI) (Wolpaw and
31 E., 2012) which is the pursuit of the development of a new channel of communication particularly aimed to
32 persons affected by neurodegenerative diseases.

33 One noteworthy aspect of this novel communication channel is the ability to transmit information from
34 the Central Nervous System (CNS) to a computer device and from there use that information to control a
35 wheelchair (Carlson and del R. Millan, 2013), as input to a speller application (Guger et al., 2009), in a
36 Virtual Reality environment (Lotte et al., 2013) or as aiding tool in a rehabilitation procedure (Jure et al.,
37 2016). The holly grail of BCI is to implement a new complete and alternative pathway to restore lost
38 locomotion (Wolpaw and E., 2012).

39 EEG signals are remarkably complex and have been characterized as a multichannel non-stationary
40 stochastic process. Additionally, they have high variability between different subjects and even between
41 different moments for the same subject, requiring adaptive and co-adaptive calibration and learning
42 procedures (Clerc et al., 2016). Hence, this imposes an outstanding challenge that is necessary to overcome
43 in order to extract information from raw EEG signals.

44 BCI has gained mainstream public awareness with worldwide challenge competitions like
45 Cybathlon (Riener and Seward, 2014; Novak et al., 2018) and even been broadcasted during the inauguration
46 ceremony of the 2014 Soccer World Cup. New developments have overcome the out-of-the-lab high-bar
47 and they are starting to be used in real world environments (Guger et al., 2017; Huggins et al., 2016).
48 However, they still lack the necessary robustness, and its performance is well behind any other method of
49 human computer interaction, including any kind of detection of residual muscular movement (Clerc et al.,
50 2016).

51 A few works have explored the idea of exploiting the signal waveform to analyze the EEG signal.
52 In (Alvarado-González et al., 2016) an approach based on Slope Horizontal Chain Code is presented,
53 whereas in (Yamaguchi et al., 2009) a similar procedure was implemented based on Mathematical
54 Morphological Analysis. The seminal work of Bandt-Pompe Permutation Entropy (Berger et al., 2017) also
55 explores succinctly this idea as a basis to establish the time series ordinal patterns. In the article (Ramele
56 et al., 2016), the authors introduce a method for classification of rhythmic EEG events like Visual Occipital
57 Alpha Waves and Motor Imagery Rolandic Central μ Rhythms using the Histogram of Gradient Orientations
58 of signal plots. Inspired in that work, we propose a novel application of the developed method to classify
59 and describe transient events, particularly the P300 Event Related Potential. The proposed approach is
60 based on the waveform analysis of the shape of the EEG signal. The signal is drawn on a bidimensional
61 image plot, vector gradients of pixels around the plot are obtained, and with them, the histogram of their
62 orientations is calculated. This histogram is a direct representation of the waveform of the signal. The
63 method is built by mimicking what regularly electroencephalographers have been performing for almost a
64 century as it is described in (Hartman, 2005): visually inspecting raw signal plots.

65 This paper reports a method to, (1) describe a procedure to capture the shape of a waveform of an ERP
66 component, the P300, using histograms of gradient orientations extracted from images of signal plots,
67 and (2) outline the way in which this procedure can be used to implement an P300-Based BCI Speller
68 application. Its validity is verified by offline processing two datasets, one of data from ALS patients and
69 another one from data of healthy subjects.

70 This article unfolds as follows: Section 2.1 is dedicated to explain the Feature Extraction method based
71 on Histogram of Gradient Orientations of the Signal Plot: Section 2.1.1 shows the preprocessing pipeline,
72 Section 2.1.2 describes the image generation of the signal plot, Section 2.1.3 presents the feature extraction

73 procedure while Section 2.1.4 introduces the Speller Matrix Letter Identification procedure. In Section 2.2,
74 the experimental protocol is expounded. Section 3 shows the results of applying the proposed technique. In
75 the final Section 4 we expose our remarks, conclusions and future work.

2 MATERIALS AND METHODS

76 The P300 (Farwell and Donchin, 1988; Knuth et al., 2006) is a positive deflection of the EEG signal which
77 occurs around 300 ms after the onset of a rare and deviant stimulus that the subject is expected to attend. It
78 is produced under the oddball paradigm (Wolpaw and E., 2012) and it is consistent across different subjects.
79 It has a lower amplitude ($\pm 5\mu V$) compared to basal EEG activity, reaching a Signal to Noise Ratio (SNR)
80 of around -15 db estimated based on the amplitude of the P300 response signal divided by the standard
81 deviation of the background EEG activity (Hu et al., 2010). This signal can be used to implement a speller
82 application by means of a Speller Matrix (Farwell and Donchin, 1988). This matrix is composed of 6 rows
83 and 6 columns of numbers and letters. The subject can focus on one character of the matrix. Figure 1 shows
84 an example of the Speller Matrix used in the OpenVibe open source software (Renard et al., 2010), where
85 the flashes of rows and columns provide the deviant stimulus required to elicit this physiological response.
86 Each time a row or a column that contains the desired letter flashes, the corresponding synchronized EEG
87 signal should also contain the P300 signature and by detecting it, the selected letter can be identified.

88 2.1 Feature Extraction from Signal Plots

89 In this section, the signal preprocessing, the method for generating images from signal plots, the feature
90 extraction procedure and the Speller Matrix identification are described. Figure 2 shows a scheme of the
91 entire process.

92 2.1.1 Preprocessing Pipeline

93 The data obtained by the capturing device is digitalized and a multichannel EEG signal is constructed.
94 The 6 rows and 6 columns of the Speller Matrix are intensified providing the visual stimulus. The
95 number of a row or column is a location. A sequence of twelve randomly permuted locations l conform an
96 intensification sequence. The whole set of twelve intensifications is repeated k_a times.

- 97 • **Signal Enhancement:** This stage consists of the enhancement of the SNR of the P300 pattern above
98 the level of basal EEG. The pipeline starts by applying a notch filter to the raw digital signal, a 4th
99 degree 10 Hz lowpass Butterworth filter and finally a decimation with a Finite Impulse Response (FIR)
100 filter of order 30 from the original sampling frequency down to 16 Hz (Krusienski et al., 2006).
- 101 • **Artifact Removal:** For every complete sequence of 12 intensifications of 6 rows and 6 columns, a
102 basic artifact elimination procedure is implemented by removing the entire sequence when any signal
103 deviates above/below $\pm 70\mu V$.
- 104 • **Segmentation:** For each of the 12 intensifications of one intensification sequence, a segment S_i^l
105 of a window of t_{max} seconds of the multichannel signal is extracted, starting from the stimulus
106 onset, corresponding to each row/column intensification l and to the intensification sequence i . As
107 intensifications are permuted in a random order, the segments are rearranged corresponding to row
108 flickering, labeled 1-6, whereas those corresponding to column flickering are labeled 7-12. Two of
109 these segments should contain the P300 ERP signature time-locked to the flashing stimulus, one for
110 the row, and one for the column.

111 • **Signal Averaging:** The P300 ERP is deeply buried under basal EEG so the standard approach to
 112 identify it is by point-to-point averaging the time-locked stacked signal segments. Hence the values
 113 which are not related to, and not time-locked to the onset of the stimulus are canceled out (Liang and
 114 Bougrain, 2008).

115 This last step determines the operation of any P300 Speller. In order to obtain an improved signal
 116 in terms of its SNR, repetitions of the sequence of row/column intensification are necessary. And,
 117 at the same time, as long as more repetitions are needed, the ability to transfer information faster is
 118 diminished, so there is a trade-off that must be acutely determined.

119 The procedure to obtain the point-to-point averaged signal goes as follows:

- 120 1. Highlight randomly the rows and columns from the matrix. There is one row and one column that
 121 should match the letter selected by the subject.
- 122 2. Repeat step 1 k_a times, obtaining the $1 \leq l \leq 12$ segments $S_1^l(n, c), \dots, S_{k_a}^l(n, c)$, of the EEG
 123 signal where the variables $1 \leq n \leq n_{max}$ and $1 \leq c \leq C$ correspond to sample points and channel,
 124 respectively. The parameter C is the number of available EEG channels whereas $n_{max} = F_s t_{max}$
 125 is the segment length and F_s is the sampling frequency. The parameter k_a is the number of
 126 repetitions of intensifications and it is an input parameter of the algorithm.
- 127 3. Compute the Ensemble Average by

$$x^l(n, c) = \frac{1}{k_a} \sum_{i=1}^{k_a} S_i^l(n, c) \quad (1)$$

128 for $1 \leq n \leq n_{max}$ and for the channels $1 \leq c \leq C$. This provide an averaged signal $x^l(n, c)$ for
 129 the twelve locations $1 \leq l \leq 12$.

130 2.1.2 Signal Plotting

131 Averaged signal segments are standardized and scaled for $1 \leq n \leq n_{max}$ and $1 \leq c \leq C$ by

$$\tilde{x}^l(n, c) = \left\lfloor \gamma \frac{(x^l(n, c) - \bar{x}^l(c))}{\hat{\sigma}^l(c)} \right\rfloor \quad (2)$$

where $\gamma > 0$ is an input parameter of the algorithm and it is related to the image scale. In addition, $x^l(n, c)$ is the point-to-point averaged multichannel EEG signal for the sample point n and for channel c . Lastly,

$$\bar{x}^l(c) = \frac{1}{n_{max}} \sum_{n=1}^{n_{max}} x^l(n, c)$$

and

$$\hat{\sigma}^l(c) = \left\{ \frac{1}{n_{max} - 1} \sum_{n=1}^{n_{max}} [x^l(n, c) - \bar{x}^l(c)]^2 \right\}^{\frac{1}{2}}$$

132 are the mean and estimated standard deviation of $x^l(n, c)$, $1 \leq n \leq n_{max}$, for each channel c .

133 Consequently, a binary image $I^{(l,c)}$ is constructed according to

$$I^{(l,c)}(z_1, z_2) = \begin{cases} 255 & \text{if } z_1 = \gamma n \quad \text{and} \quad z_2 = \tilde{x}^l(n, c) + z^l(c) \\ 0 & \text{otherwise} \end{cases} \quad (3)$$

134 with 255 being white and representing the signal's value location and 0 for black which is the background
 135 contrast, conforming a black-and-white plot of the signal. Pixel arguments $(z_1, z_2) \in \mathbb{N} \times \mathbb{N}$ iterate over
 136 the width (based on the length of the signal segment) and height (based on the peak-to-peak amplitude) of
 137 the newly created image with $1 \leq n \leq n_{max}$ and $1 \leq c \leq C$. The value $z^l(c)$ is the image vertical position
 138 where the signal's zero value has to be situated in order to fit the entire signal within the image for each
 139 channel c:

$$z^l(c) = \left\lfloor \frac{\max_n \tilde{x}^l(n, c) - \min_n \tilde{x}^l(n, c)}{2} \right\rfloor - \left\lfloor \frac{\max_n \tilde{x}^l(n, c) + \min_n \tilde{x}^l(n, c)}{2} \right\rfloor \quad (4)$$

140 where the minimization and maximization are carried out for n varying between $1 \leq n \leq n_{max}$, and $\lfloor \cdot \rfloor$
 141 denote the rounding to the smaller nearest integer of the number.

142 In order to complete the plot $I^{(l,c)}$ from the pixels, the Bresenham (Bresenham, 1965; Ramele et al.,
 143 2016) algorithm is used to interpolate straight lines between each pair of consecutive pixels.

144 2.1.3 Feature Extraction: Histogram of Gradient Orientations

145 The work of Edelman, Intrator and Poggio (Edelman et al., 1997) on how the visual cortex sense features
 146 was the inspiration to the development of an algorithm to identify and decode salient local information
 147 from image regions. The Scale Invariant Feature Transform (SIFT) is a Computer Vision method proposed
 148 by Lowe (2004) which is composed of two parts, the SIFT Detector and the SIFT Descriptor. The former
 149 is the procedure to identify relevant areas of an image whereas the latter is the procedure to describe and
 150 characterize a region of an image (i.e. patch) calculating an histogram of the angular orientations of pixel
 151 gradients. In order to characterize EEG signal waveforms, this work proposes an alternative to the SIFT
 152 Descriptor, the Histogram of Gradient Orientations algorithm.

153 For each generated image $I^{(l,c)}$, a keypoint p_k is placed on a pixel (x_{p_k}, y_{p_k}) over the image plot and a
 154 window around the keypoint is considered. A local image patch of size $X_p \times X_p$ pixels is constructed by
 155 dividing the window in 16 blocks of size $3s$ each one, where s is the scale of the local patch and it is an
 156 input parameter of the algorithm. It is arranged in a 4×4 grid and the pixel p_k is the patch center, thus
 157 $X_p = 12s$ pixels.

158 A local representation of the signal shape within the patch can be described by obtaining the gradient
 159 orientations on each of the 16 blocks $B_{i,j}$ with $0 \leq i, j \leq 3$ and creating a histogram of gradients. In
 160 order to calculate the histogram, the interval $[0, 360]$ of possible angles is divided in 8 bins, each one of 45
 161 degrees.

162 Hence, for each spatial bin $0 \leq i, j \leq 3$, corresponding to the indexes of each block $B_{i,j}$, the orientations
 163 are accumulated in a 3-dimensional histogram h through the following equation:

$$h(\theta, i, j) = 3s \sum_{\mathbf{p} \in I^{(l,c)}} w_{ang}(\angle J(\mathbf{p}) - \theta) w_{ij} \left(\frac{\mathbf{p} - \mathbf{p}_k}{3s} \right) \|J(\mathbf{p})\| \quad (5)$$

164 where \mathbf{p} is a pixel from the image $I^{(l,c)}$, θ is the angle bin with $\theta \in \{0, 45, 90, 135, 180, 225, 270, 315\}$,
 165 $\|J(\mathbf{p})\|$ is the norm of the gradient vector in the pixel \mathbf{p} and it is computed using finite differences and
 166 $\angle J(\mathbf{p})$ is the angle of the gradient vector.

167 The contribution of each gradient vector to the histogram calculated by Equation 5 is balanced by a
 168 trilinear interpolation. The scalar $w_{ang}(\cdot)$ and vector $w_{ij}(\cdot)$ functions are linear interpolations used by Lowe
 169 (2004) and Vedaldi and Fulkerson (2010) to provide a weighting contribution to the eight adjacent bins in
 170 the tridimensional histogram. They are calculated as

$$w_{ij}(\mathbf{v}) = w(v_x - x_i)w(v_y - y_j) \quad (6)$$

171 with $0 \leq i, j \leq 3$ and

$$w_{ang}(\alpha) = \sum_{r=-1}^1 w\left(\frac{8\alpha}{2\pi} + 8r\right) \quad (7)$$

172 where x_i and y_i are the spatial bin centers located in $x_i, y_i \in \{-\frac{3}{2}, -\frac{1}{2}, \frac{1}{2}, \frac{3}{2}\}$ and the interpolating function
 173 $w(\cdot)$ is defined as $w(z) = \max(0, 1 - |z|)$. The function parameter $\mathbf{v} = (v_x, v_y)$ is a vector variable and α
 174 a scalar variable. Vector \mathbf{v} holds pixel coordinates (v_x, v_y) normalized between -2 and 2 and combined
 175 with the function $w(z)$ it produces zero for every combination of (i, j) except for the 4 adjacent spatial
 176 bins. On the other hand, r is an integer that can vary freely in the set $\{-1, 0, 1\}$ and α is the difference
 177 between the gradient orientation angle and the angle bin center in radians. By following this procedure,
 178 summands on Equation 7 are nullified except for the 2 adjacent angular bins.

179 These binning functions conform the trilinear interpolation that has a combined effect of sharing the
 180 contribution of each oriented gradient between their eight adjacent bins in a tridimensional cube in the
 181 histogram space, and zero everywhere else (Mortensen et al., 2005).

182 The fixed value of 3 is a magnification factor which corresponds to the number of pixels per each
 183 block when $s = 1$. As the patch has 16 blocks and 8 bin angles are considered, for each location l and
 184 channel c a feature called *descriptor* $\mathbf{d}^{(l,c)}$ of 128 dimension is obtained. The main differences between
 185 this implementation and the standard SIFT Descriptor are described in the Appendix on Section 5.

186 Figure 3 shows an example of a patch and a scheme of the histogram computation. In (A) a plot of the
 187 signal and the patch centered around the keypoint is shown. In (B) the possible orientations on each patch
 188 are illustrated. Only the upper-left four blocks are visible. The first eight orientations of the first block, are
 189 labeled from 1 to 8 clockwise. The orientations of the second block $B_{1,2}$ are labeled from 9 to 16. This
 190 labeling continues left-to-right, up-down until the eight orientations for all the sixteen blocks are assigned.
 191 They form the corresponding descriptor \mathbf{d} of 128 coordinates. Finally, in (C) an enlarged image plot is
 192 shown where the oriented gradient vector for each pixel can be seen.

193 2.1.4 Speller Matrix letter Identification

194 2.1.4.1 P300 ERP Extraction

195 Segments corresponding to row flickering are labeled 1-6, whereas those corresponding to column
 196 flickering are labeled 7-12. The extraction process has the following steps:

- **Step A:** First highlight rows and columns from the matrix in a random permutation order and obtain the Ensemble Average as detailed in steps 1, 2 and 3 in Section 2.1.1.
- **Step B:** Plot the signals $\tilde{x}^l(n, c)$, $1 \leq n \leq n_{max}$, $1 \leq c \leq C$, according Section 2.1.2 in order to generate the images $I^{(l,c)}$ for rows and columns $1 \leq l \leq 12$.
- **Step C:** Obtain the descriptors $\mathbf{d}^{(l,c)}$ for rows and columns from $I^{(l,c)}$ in accordance to the method described in Section 2.1.3.

2.1.4.2 Calibration

A trial, as defined by the BCI2000 platform (Schalk et al., 2004), is every attempt to select just one letter from the speller. A set of trials is used for calibration and once the calibration is complete it can be used to identify new letters from new trials.

During the calibration phase, two descriptors $\mathbf{d}^{(l,c)}$ are extracted for each available channel, corresponding to the locations l of a selection of one previously instructed letter from the set of calibration trials. These descriptors are the P300 templates, grouped together in a template set called T^c . The set is constructed using the steps described in Section 2.1.1 and the steps A, B and C of the P300 ERP extraction process.

Additionally, the best performing channel, bpc is identified based on the the channel where the best Character Recognition Rate is obtained.

2.1.4.3 Letter identification

In order to identify the selected letter, the template set T^{bpc} is used as a database. Thus, new unclassified descriptors $\mathbf{q}^{(l,bpc)}$ are computed and they are compared against the descriptors belonging to the calibration template set T^{bpc} .

The Naive Bayes Nearest Neighbor (k-NBNN) (Boiman et al., 2008) is a discriminative (Wolpaw and E., 2012) semi-supervised classification algorithm that allows the categorization of an image to one class by comparing the set of extracted descriptors to those which are more similar from template dictionaries. This work proposes an adapted version to obtain a unary classification scheme to identify the selected letter in the P300-Based BCI Speller, based on the features provided by the calculated descriptors.

• **Step D:** Match to the calibration template T^{bpc} by computing

$$\hat{row} = \arg \min_{l \in \{1, \dots, 6\}} \sum_{h=1}^k \left\| \mathbf{q}^{(l,bpc)} - \mathbf{d}_h^{(bpc)} \right\|^2 \quad (8)$$

and

$$\hat{col} = \arg \min_{l \in \{7, \dots, 12\}} \sum_{h=1}^k \left\| \mathbf{q}^{(l,bpc)} - \mathbf{d}_h^{(bpc)} \right\|^2 \quad (9)$$

with $\mathbf{d}_h^{(bpc)}$ belonging to the set $N_T(\mathbf{q}^{(l,bpc)})$, which is defined, for the best performing channel, as $N_T(\mathbf{q}^{(l,bpc)}) = \{\mathbf{d}_h^{(bpc)} \in T^{bpc} / \mathbf{d}_h^{(bpc)} \text{ is the } k\text{-nearest neighbor of } \mathbf{q}^{(l,bpc)}\}$. This set is obtained by sorting all the elements in T^{bpc} based on distances between them and $\mathbf{q}^{(l,bpc)}$, choosing the k with smaller values, with k a parameter of the algorithm.

By computing the aforementioned equations, the letter of the matrix can be determined from the intersection of the row \hat{row} and column \hat{col} . Figure 2 shows a scheme of this process.

230 2.2 Experimental Protocol

231 To verify the validity of the proposed framework and method, the public dataset 008-2014 (Riccio et al.,
232 2013) published on the BNCI-Horizon website (Brunner et al., 2014) by IRCCS Fondazione Santa Lucia,
233 is used. Additionally, an own dataset with the same experimental conditions is generated. Both of them are
234 utilized to perform an offline BCI Simulation to decode the spelled words from the provided signals.

235 The algorithm is implemented on MATLAB V2017a (Mathworks Inc., Natick, MA, USA). The algorithm
236 described in 2.1.3 is implemented on a modified version of the VLFeat (Vedaldi and Fulkerson, 2010)
237 Computer Vision library. Furthermore, in order to enhance the impact of this paper and for a sake of
238 reproducibility, the code of the entire algorithm, including the modified VLFeat library, has been made
239 available at: <https://bitbucket.org/itba/hist>.

240 In the following sections the characteristics of the datasets and parameters of the identification algorithm
241 are described.

242 2.2.1 P300 ALS Public Dataset

243 The experimental protocol used to generate this dataset is explained in (Riccio et al., 2013) but can
244 be summarized as follows: 8 subjects with confirmed diagnoses but on different stages of ALS disease,
245 were recruited and accepted to perform the experiments. The Visual P300 detection task designed for this
246 experiment consisted of spelling 7 words of 5 letters each, using the traditional P300 Speller Matrix (Farwell
247 and Donchin, 1988). The flashing of rows and columns provide the deviant stimulus required to elicit this
248 physiological response. The first 3 words are used for calibration and the remaining 4 words, for testing
249 with visual feedback. A trial is every attempt to select a letter from the speller. It is composed of signal
250 segments corresponding to $k_a = 10$ repetitions of flashes of 6 rows and $k_a = 10$ repetitions of flashes of 6
251 columns of the matrix, yielding 120 repetitions. Flashing of a row or a column is performed for 0.125s,
252 following by a resting period (i.e. inter-stimulus interval) of the same length. After 120 repetitions an
253 inter-trial pause is included before resuming with the following letter.

254 The recorded dataset was sampled at 256 Hz and it consisted of a scalp multichannel EEG signal for
255 electrode channels Fz, Cz, Pz, Oz, P3, P4, PO7 and PO8, identified according to the 10-20 International
256 System, for each one of the 8 subjects. The recording device was a research-oriented digital EEG device
257 (g.Mobilab, g.Tec, Austria) and the data acquisition and stimuli delivery were handled by the BCI2000
258 open source software (Schalk et al., 2004).

259 In order to assess and verify the identification of the P300 response, subjects are instructed to perform a
260 copy-spelling task. They have to fix their attention to successive letters for copying a previously determined
261 set of words, in contrast to a free-running operation of the speller where each user decides on its own what
262 letter to choose.

263 2.2.2 P300 for healthy subjects

264 We replicate the same experiment on healthy subjects using a wireless digital EEG device (g.Nautilus,
265 g.Tec, Austria). The experimental conditions are the same as those used for the previous dataset, as detailed
266 in section 2.2.1. The produced dataset is available in a public online repository (Ramele et al., 2017).

267 Participants are recruited voluntarily and the experiment is conducted anonymously in accordance with
268 the Declaration of Helsinki published by the World Health Organization. No monetary compensation
269 is handed out and all participants agree and sign a written informed consent. This study is approved
270 by the *Departamento de Investigación y Doctorado, Instituto Tecnológico de Buenos Aires (ITBA)*. All

271 healthy subjects have normal or corrected-to-normal vision and no history of neurological disorders. The
 272 experiment is performed with 8 subjects, 6 males, 2 females, 6 right-handed, 2 left-handed, average age
 273 29.00 years, standard deviation 11.56 years, range 20-56 years.

274 EEG data is collected in a single recording session. Participants are seated in a comfortable chair, with
 275 their vision aligned to a computer screen located one meter in front of them. The handling and processing
 276 of the data and stimuli is conducted by the OpenVibe platform (Renard et al., 2010).

277 Gel-based active electrodes (g.LADYbird, g.Tec, Austria) are used on the same positions Fz, Cz, Pz,
 278 Oz, P3,P4, PO7 and PO8. Reference is set to the right ear lobe and ground is preset as the AFz position.
 279 Sampling frequency is slightly different, and is set to 250 Hz, which is the closest possible to the one used
 280 with the other dataset.

281 2.2.3 Parameters

282 The patch size is $X_P = 12s \times 12s$ pixels, where s is the scale of the local patch and it is an input parameter
 283 of the algorithm. The P300 event can have a span of 400 ms and its amplitude can reach $10\mu V$ (Rao, 2013).
 284 Hence it is necessary to utilize a signal segment of size $t_{max} = 1$ second and a size patch X_P that could
 285 capture an entire transient event. With this purpose in consideration, the s value election is essential.

286 We propose the Equations 10 and 11 to compute the scale value in horizontal and vertical directions,
 287 respectively.

$$s_x = \frac{\gamma \lambda F_s}{12} \quad (10)$$

$$s_y = \frac{\gamma \Delta\mu V}{12} \quad (11)$$

288 where λ is the length in seconds covered by the patch, F_s is the sampling frequency of the EEG signal
 289 (downsampled to 16 Hz) and $\Delta\mu V$ corresponds to the amplitude in microvolts that can be covered by the
 290 height of the patch. The geometric structure of the patch is determined by the waveform to be captured,
 291 thus we discerned that by using $s = s_x = s_y = 3$ and $\gamma = 4$, the local patch and the descriptor can identify
 292 events of $9\mu V$ of amplitude, with a span of $\lambda = 0.56$ seconds. This also determines that 1 pixel represents
 293 $\frac{1}{\gamma} = \frac{1}{4}\mu V$ on the vertical direction and $\frac{1}{F_s \gamma} = \frac{1}{64}$ seconds on the horizontal direction. The keypoints p_k
 294 are located at $(x_{p_k}, y_{p_k}) = (0.55F_s \gamma, z^l(c)) = (35, z^l(c))$ for the corresponding channel c and location l
 295 (see Equation 4). In this way the whole transient event is captured. Figure 4 shows a patch of a signal plot
 296 covering the complete amplitude (vertical direction) and the complete span of the signal event (horizontal
 297 direction).

298 The number of channels C is equal to 8 for both datasets, and the number of intensification sequences k_a
 299 is fixed to 10. The parameter k used to construct the set $N_T(\mathbf{q}^{(l,c)})$ is assigned to $k = 7$, which was found
 300 empirically to achieve better results. In addition, the norm used on Equations 8 and 9 is the cosine norm,
 301 and descriptors are normalized to $[-1, 1]$.

302 Lastly, in order to assess the validity of the Histogram of Gradient Orientations (HIST) method, the
 303 character recognition rate for both datasets is evaluated replicating the methodology proposed by the
 304 ALS dataset's publisher, since authors Riccio et al. (2013) did not report the Character Recognition
 305 Rate obtained for this dataset. Frequency filtering, data segmentation and artifact rejection is conducted
 306 according to Section 2.1.1 yielding 16×8 samples per epoch. A multichannel feature consists of time
 307 points vector (Lotte et al., 2018), formed by concatenating all the channels (Krusienski et al., 2006). A

single-channel variant consists of using time points from a single electrode and performing the analysis on a channel-by-channel basis. Three classification schemes are considered as well. A multichannel version of the Stepwise Linear Discriminant Analysis (SWLDA) classification algorithm. SWLDA is the methodology proposed by the ALS dataset's publisher. Additionally, a single-channel and a multichannel variant of a linear kernel Support Vector Machine (SVM) (Scholkopf and Smola, 2001) classifier are utilized. SVM has been successfully used in several BCI Competitions (Rakotomamonjy and Guigue, 2008).

3 RESULTS

Table 1 shows the results of applying the HIST algorithm to the subjects of the public dataset of ALS patients. The percentage of correctly spelled letters is calculated while performing an offline BCI Simulation. From the seven words for each subject, the first three are used for calibration, and the remaining four are used for testing. The best performing channel *bpc* is informed as well. The target ratio is 1 : 36; hence theoretical chance level is 2.8%. It can be observed that the best performance of the letter identification method is reached in a dissimilar channel depending on the subject being studied. Table 1 and 2 show for comparison the obtained performance rates using single-channel signals with the SVM classifier. The best performing channel, where the best letter identification rate was achieved, is also depicted.

The Information Transfer Rate (ITR), or Bit Transfer Rate (BTR), in the case of reactive BCIs (Wolpaw and E., 2012) depends on the amount of signal averaging required to transmit a valid and robust selection. Figure 5 shows the performance curves for varying intensification sequences for the subjects included in the dataset of ALS patients. It can be noticed that the percentage of correctly identified letters depends on the number of intensification sequences that are used to obtain the averaged signal. Moreover, when the number of intensification sequences tend to 1, which corresponds to single-intensification character recognition, the performance is reduced. As mentioned before, the SNR of the P300 obtained from only one segment of the intensification sequence is very low and the shape of its P300 component is not very well defined.

In Table 2 the results obtained for 8 healthy subjects are shown. It can be observed that the performance is above chance level. It is verified that HIST method has an improved performance at letter identification than SVM that process the signals on a channel by channel strategy (Wilcoxon signed-rank test, $p = 0.004$ for both datasets).

Tables 3 and 4 are presented in order to compare the performance of the HIST method versus multichannel SWLDA and SVM classification algorithms for both datasets. It is verified for the dataset of ALS patients that it has similar performance against other methods like SWLDA or SVM, which use a multichannel feature (Quade test with $p = 0.55$) whereas for the dataset of healthy subjects significant differences are found (Quade test with $p = 0.02$) where only the HIST method achieves a different performance than SVM (with multiple comparisons, significant difference of level 0.05).

The P300 ERP consists of two overlapping components: the P3a and P3b, the former with frontocentral distribution while the later stronger on centroparietal region (Polich, 2007). Hence, the standard practice is to find the stronger response on the central channel Cz (Riccio et al., 2013). However, Krusienski et al. (2006) show that the response may also arise in occipital regions. We found that by analyzing only the waveforms, occipital channels PO8 and PO7 show higher performances for some subjects.

As subjects have varying *latencies* and *amplitudes* of their P300 components, they also have a varying stability of the *shape* of the generated ERP (Nam et al., 2010). Figure 6 shows 10 sample P300 templates patches for patients 8 and 3 from the dataset of ALS patients. It can be discerned that in coincidence with

349 the performance results, the P300 signature is more clear and consistent for subject 8 (A) while for subject
350 3 (B) the characteristic pattern is more difficult to perceive.

351 Additionally, the stability of the P300 component waveform has been extensively studied in patients
352 with ALS (Sellers et al., 2006; Madarame et al., 2008; Nijboer and Broermann, 2009; Mak et al., 2012;
353 McCane et al., 2015) where it was found that these patients have a stable P300 component, which were
354 also sustained across different sessions. In line with these results we do not find evidence of a difference in
355 terms of the performance obtained by analyzing the waveforms (HIST) for the group of patients with ALS
356 and the healthy group of volunteers (Mann-Whitney U Test, $p = 0.46$). Particularly, the best performance
357 is obtained for a subject from the ALS dataset for which, based on visual observation, the shape of their
358 P300 component is consistently identified.

359 It is important to remark that when applied to binary images obtained from signal plots, the feature
360 extraction method described in Section 2.1.3 generates sparse descriptors. Under this subspace we found
361 that using the cosine metric yielded a significant performance improvement. On the other hand, the unary
362 classification scheme based on the NBNN algorithm proved very beneficial for the P300 Speller Matrix.
363 This is due to the fact that this approach solves the unbalance dataset problem which is inherent to the
364 oddball paradigm (Tibon and Levy, 2015).

4 DISCUSSION

365 Among other applications of Brain Computer Interfaces, the goal of the discipline is to provide
366 communication assistance to people affected by neuro-degenerative diseases, who are the most likely
367 population to benefit from BCI systems and EEG processing and analysis.

368 In this work, a method to extract an objective metric from the waveform of the plots of EEG signals is
369 presented. Its usage to implement a valid P300-Based BCI Speller application is expounded. Additionally,
370 its validity is evaluated using a public dataset of ALS patients and an own dataset of healthy subjects.

371 It was verified that this method has an improved performance at letter identification than other methods
372 that process the signals on a channel by channel strategy, and it even has a comparable performance against
373 other methods like SWLDA or SVM, which uses a multichannel feature. Furthermore, this method has the
374 advantage that shapes of waveforms can be analyzed in an objective way. We observed that the shape of
375 the P300 component is more stable in occipital channels, where the performance for identifying letters
376 is higher. We additionally verified that ALS P300 signatures are stable in comparison to those of healthy
377 subjects.

378 We believe that the use of descriptors based on histogram of gradient orientation, presented in this work,
379 can also be utilized for deriving a shape metric in the space of the P300 signals which can complement
380 other metrics based on time-domain as those defined by Mak et al. (2012). It is important to notice
381 that the analysis of waveform shapes is usually performed in a qualitative approach based on visual
382 inspection (Sellers et al., 2006), and a complementary methodology which offer a quantitative metric will
383 be beneficial to these routine analysis of the waveform of ERPs.

384 The goal of this work is to answer the question if a P300 component could be solely determined by
385 inspecting automatically their waveforms. We conclude affirmatively, though two very important issues
386 still remain:

387 First, the stability of the P300 in terms of its shape is crucial: the averaging procedure, montages, the
388 signal to noise ratio and spatial filters all of them are non-physiological factors that affect the stability of

389 the shape of the P300 ERP. We tested a preliminary approach to assess if the morphological shape of the
390 P300 of the averaged signal can be stabilized by applying different alignments of the stacked segments (see
391 Figure 2) and we verified that there is a better performance when a correct segment alignment is applied.
392 We applied Dynamic Time Warping (DTW) (Casarotto et al., 2005) to automate the alignment procedure
393 but we were unable to find a substantial improvement. Further work to study the stability of the shape of
394 the P300 signature component needs to be addressed.

395 The second problem is the amplitude variation of the P300. We propose a solution by standardizing the
396 signal, shown in Equation 2. It has the effect of normalizing the peak-to-peak amplitude, moderating its
397 variation. It has also the advantage of reducing noise that was not reduced by the averaging procedure. It is
398 important to remark that the averaged signal variance depends on the number of segments used to compute
399 it (Van Drongelen, 2006). The standardizing process converts the signal to unit signal variance which
400 makes it independent of the number k_a of signals averaged. Although this is initially an advantageous
401 approach, the standardizing process reduces the amplitude of any significant P300 complex diminishing its
402 automatic interpretation capability.

403 To further extend the capabilities of this method, it would be desirable to implement a multichannel
404 version. The straightforward extension of concatenating the obtained descriptors results in high dimensional
405 feature vector, while other variants that merge descriptors per channel may diminish the mutual information
406 between different channels. Hitherto variants using color versions of SIFT (Van De Sande et al., 2010),
407 where different color bands are mapped to electrode channels, have been explored without substantial
408 success.

409 In our opinion, the best benefit of the presented method is that a closer collaboration of the field of BCI
410 with physicians can be fostered (Chavarriaga et al., 2017), since this procedure intent to imitate human
411 visual observation. Automatic classification of patterns in EEG that are specifically identified by their
412 shapes like K-Complex, Vertex Waves, Positive Occipital Sharp Transient (Hartman, 2005) are a prospect
413 future work to be considered. We are currently working in unpublished material analyzing K-Complex
414 components that could eventually provide assistance to physicians to locate these EEG patterns, specially in
415 long recording periods, frequent in sleep research (Michel and Murray, 2012). Additionally, it can be used
416 for artifact removal which is performed on many occasions by visually inspecting signals. This is due to
417 the fact that the descriptors are a direct representation of the shape of signal waveforms. In line with these
418 applications, it can be used to build a database (Chavarriaga et al., 2017) of quantitative representations of
419 waveforms and improve atlases (Hartman, 2005), which are currently based on qualitative descriptions of
420 signal shapes.

CONFLICT OF INTEREST STATEMENT

421 The authors declare that the research was conducted in the absence of any commercial or financial
422 relationships that could be construed as a potential conflict of interest.

AUTHOR CONTRIBUTIONS

423 This work is part of the PhD thesis of RR which is directed by JS and codirected by AV.

FUNDING

424 This project was supported by the ITBACyT-15 funding program issued by ITBA University from Buenos
425 Aires, Argentina.

REFERENCES

- 426 Alvarado-González, M., Garduño, E., Bribiesca, E., Yáñez-Suárez, O., and Medina-Bañuelos, V. (2016).
427 P300 Detection Based on EEG Shape Features. *Computational and Mathematical Methods in Medicine*,
428 1–14doi:10.1155/2016/2029791
- 429 Arandjelovic, R. and Zisserman, A. (2012). Three things everyone should know to improve object
430 retrieval. In *2012 IEEE Conference on Computer Vision and Pattern Recognition(CVPR)*. 2911–2918.
431 doi:10.1109/CVPR.2012.6248018
- 432 Berger, S., Schneider, G., Kochs, E., and Jordan, D. (2017). Permutation Entropy: Too Complex a Measure
433 for EEG Time Series? *Entropy 2017, Vol. 19, Page 692* 19, 692. doi:10.3390/E19120692
- 434 Boiman, O., Shechtman, E., and Irani, M. (2008). In defense of nearest-neighbor based image classification.
435 *26th IEEE Conference on Computer Vision and Pattern Recognition, CVPR* doi:10.1109/CVPR.2008.
436 4587598
- 437 Bresenham, J. E. (1965). Algorithm for computer control of a digital plotter. *IBM Systems Journal* 4,
438 25–30
- 439 Brunner, C., Blankertz, B., Cincotti, F., Kübler, A., Mattia, D., Miralles, F., et al. (2014). BNCI Horizon
440 2020 – Towards a Roadmap for Brain / Neural Computer Interaction. *Lecture Notes in Computer Science*
441 8513, 475–486
- 442 Carlson, T. and del R. Millan, J. (2013). Brain-controlled wheelchairs: A robotic architecture. *IEEE*
443 *Robotics & Automation Magazine* 20, 65–73. doi:10.1109/MRA.2012.2229936
- 444 Casarotto, S., Bianchi, A., Cerutti, S., and Chiarenza, G. (2005). Dynamic time warping in the analysis of
445 event-related potentials. *IEEE Engineering in Medicine and Biology Magazine* 24, 68–77. doi:10.1109/
446 MEMB.2005.1384103
- 447 Chavarriaga, R., Fried-Oken, M., Kleih, S., Lotte, F., and Scherer, R. (2017). Heading for new shores!
448 Overcoming pitfalls in BCI design. *Brain-Computer Interfaces* 4, 60–73. doi:10.1080/2326263X.2016.
449 1263916
- 450 Clerc, M., Bougrain, L., and Lotte, F. (2016). *Brain-computer interfaces, Technology and applications*
451 2(*Cognitive Science*) (ISTE Ltd. and Wiley)
- 452 De Vos, M. and Debener, S. (2014). Mobile EEG: Towards brain activity monitoring during natural action
453 and cognition. *International Journal of Psychophysiology* 91, 1–2. doi:10.1016/j.ijpsycho.2013.10.008
- 454 Edelman, S., Intrator, N., and Poggio, T. (1997). Complex cells and object recognition
- 455 Farwell, L. A. and Donchin, E. (1988). Talking off the top of your head: toward a mental prosthesis utilizing
456 event-related brain potentials. *Electroencephalography and clinical neurophysiology* 70, 510–23
- 457 Guger, C., Allison, B. Z., and Lebedev, M. A. (2017). Introduction. In *Brain Computer Interface Research: A State of the Art Summary* 6 (Springer, Cham). 1–8. doi:10.1007/978-3-319-64373-1_1
- 458 Guger, C., Daban, S., Sellers, E., Holzner, C., Krausz, G., Carabalona, R., et al. (2009). How many people
459 are able to control a P300-based brain-computer interface (BCI)? *Neuroscience Letters* 462, 94–98.
460 doi:10.1016/j.neulet.2009.06.045
- 461 Hartman, a. L. (2005). *Atlas of EEG Patterns*, vol. 65 (Lippincott Williams & Wilkins). doi:10.1212/01.
462 wnl.0000174180.41994.39

- 464 Hu, L., Mouraux, A., Hu, Y., and Iannetti, G. D. (2010). A novel approach for enhancing the signal-to-noise
465 ratio and detecting automatically event-related potentials (ERPs) in single trials. *NeuroImage* 50, 99–111.
466 doi:10.1016/j.neuroimage.2009.12.010
- 467 Huggins, J. E., Alcaide-Aguirre, R. E., and Hill, K. (2016). Effects of text generation on P300 brain-
468 computer interface performance. *Brain-Computer Interfaces* 3, 112–120. doi:10.1080/2326263X.2016.
469 1203629
- 470 Jure, F., Carrere, L., Gentiletti, G., and Tabernig, C. (2016). BCI-FES system for neuro-rehabilitation of
471 stroke patients. *Journal of Physics: Conference Series* 705, 1–8. doi:10.1088/1742-6596/705/1/012058
- 472 Knuth, K. H., Shah, A. S., Truccolo, W. A., Ding, M., Bressler, S. L., and Schroeder, C. E. (2006).
473 Differentially variable component analysis: Identifying multiple evoked components using trial-to-trial
474 variability. *Journal of Neurophysiology* 95, 3257–3276. doi:10.1152/jn.00663.2005
- 475 Krusienski, D. J., Sellers, E. W., Cabestany, F., Bayoudh, S., McFarland, D. J., Vaughan, T. M., et al.
476 (2006). A comparison of classification techniques for the P300 Speller. *Journal of Neural Engineering*
477 3, 299–305. doi:10.1088/1741-2560/3/4/007
- 478 Liang, N. and Bougrain, L. (2008). Averaging techniques for single-trial analysis of oddball event-related
479 potentials. *4th International Brain-Computer*, 1–6
- 480 Lotte, F., Bougrain, L., Cichocki, A., Clerc, M., Congedo, M., Rakotomamonjy, A., et al. (2018). A review
481 of classification algorithms for EEG-based brain–computer interfaces: a 10 year update. *Journal of*
482 *Neural Engineering* 15, 031005. doi:10.1088/1741-2552/aab2f2
- 483 Lotte, F., Faller, J., Guger, C., Renard, Y., Pfurtscheller, G., Lécuyer, A., et al. (2013). *Combining BCI*
484 *with Virtual Reality: Towards New Applications and Improved BCI* (Berlin, Heidelberg: Springer Berlin
485 Heidelberg). 197–220. doi:10.1007/978-3-642-29746-5_10
- 486 Lowe, G. (2004). SIFT - The Scale Invariant Feature Transform. *International Journal* 2, 91–110
- 487 Madarame, T., Tanaka, H., Inoue, T., Kamata, M., and Shino, M. (2008). The development of a brain
488 computer interface device for amyotrophic lateral sclerosis patients. In *Conference Proceedings - IEEE*
489 *International Conference on Systems, Man and Cybernetics* (IEEE), 2401–2406. doi:10.1109/ICSMC.
490 2008.4811654
- 491 Mak, J. N., McFarland, D. J., Vaughan, T. M., McCane, L. M., Tsui, P. Z., Zeitlin, D. J., et al. (2012). EEG
492 correlates of P300-based brain-computer interface (BCI) performance in people with amyotrophic lateral
493 sclerosis. *Journal of Neural Engineering* 9. doi:10.1088/1741-2560/9/2/026014
- 494 McCane, L. M., Heckman, S. M., McFarland, D. J., Townsend, G., Mak, J. N., Sellers, E. W., et al.
495 (2015). P300-based brain-computer interface (BCI) event-related potentials (ERPs): People with
496 amyotrophic lateral sclerosis (ALS) vs. age-matched controls. *Clinical Neurophysiology* 126, 2124–2131.
497 doi:10.1016/j.clinph.2015.01.013
- 498 Michel, C. M. and Murray, M. M. (2012). Towards the utilization of EEG as a brain imaging tool.
499 *NeuroImage* 61, 371–385. doi:10.1016/j.neuroimage.2011.12.039
- 500 Mortensen, E. N., , and Shapiro, L. (2005). A sift descriptor with global context. In *2005 IEEE*
501 *Computer Society Conference on Computer Vision and Pattern Recognition (CVPR'05)*. vol. 1, 184–190.
502 doi:10.1109/CVPR.2005.45
- 503 Nam, C. S., Li, Y., and Johnson, S. (2010). Evaluation of P300-based brain-computer interface in real-
504 world contexts. *International Journal of Human-Computer Interaction* 26, 621–637. doi:10.1080/
505 10447311003781326
- 506 Nijboer, F. and Broermann, U. (2009). Brain Computer Interfaces for Communication and Control in
507 Locked-in Patients. In *Graimann B., Pfurtscheller G., Allison B. (eds) Brain-Computer Interfaces. The*
508 *Frontiers Collection*. (Springer Berlin Heidelberg). 185–201. doi:10.1007/978-3-642-02091-9_11

- 509 Novak, D., Sigrist, R., Gerig, N. J., Wyss, D., Bauer, R., Gotz, U., et al. (2018). Benchmarking brain-
510 computer interfaces outside the laboratory: The cybathlon 2016. *Frontiers in Neuroscience* 11, 756.
511 doi:10.3389/fnins.2017.00756
- 512 Polich, J. (2007). Updating P300: An integrative theory of P3a and P3b. *Clinical Neurophysiology* 118,
513 2128–2148. doi:10.1016/j.clinph.2007.04.019
- 514 Rakotomamonjy, A. and Guigue, V. (2008). BCI Competition III: Dataset II- Ensemble of SVMs for BCI
515 P300 Speller. *IEEE Transactions on Biomedical Engineering* 55, 1147–1154. doi:10.1109/TBME.2008.
516 915728
- 517 Ramele, R., Villar, A. J., and Santos, J. M. (2016). BCI classification based on signal plots and SIFT
518 descriptors. In *4th International Winter Conference on Brain-Computer Interface, BCI 2016* (Yongpyong:
519 IEEE), 1–4. doi:10.1109/IWW-BCI.2016.7457454
- 520 [Dataset] Ramele, R., Villar, A. J., and Santos, J. M. (2017). P300-dataset rrid scr_015977.
521 <https://www.kaggle.com/rramele/p300samplingdataset>
- 522 Rao, R. P. N. (2013). *Brain-Computer Interfacing: An Introduction* (New York, NY, USA: Cambridge
523 University Press)
- 524 Renard, Y., Lotte, F., Gibert, G., Congedo, M., Maby, E., Delannoy, V., et al. (2010). OpenViBE: An
525 Open-Source Software Platform to Design, Test, and Use Brain–Computer Interfaces in Real and Virtual
526 Environments. *Presence: Teleoperators and Virtual Environments* 19, 35–53. doi:10.1162/pres.19.1.35
- 527 Rey-Otero, I. and Delbracio, M. (2014). Anatomy of the SIFT Method. *Image Processing On Line* ,
528 370–396doi:<http://dx.doi.org/10.5201/ipol.2014.82>
- 529 Riccio, A., Simione, L., Schettini, F., Pizzimenti, A., Inghilleri, M., Belardinelli, M. O., et al. (2013).
530 Attention and P300-based BCI performance in people with amyotrophic lateral sclerosis. *Frontiers in
531 Human Neuroscience* 7, 732. doi:10.3389/fnhum.2013.00732
- 532 Riener, R. and Seward, L. J. (2014). Cybathlon 2016. *2014 IEEE International Conference on Systems,
533 Man, and Cybernetics (SMC)* , 2792–2794doi:10.1109/SMC.2014.6974351
- 534 Schalk, G., McFarland, D. J., Hinterberger, T., Birbaumer, N., and Wolpaw, J. R. (2004). BCI2000: a
535 general-purpose brain-computer interface (BCI) system. *IEEE transactions on bio-medical engineering*
536 51, 1034–43. doi:10.1109/TBME.2004.827072
- 537 Scholkopf, B. and Smola, A. J. (2001). *Learning with kernels: support vector machines, regularization,
538 optimization, and beyond* (MIT press)
- 539 Schomer, D. L. and Silva, F. L. D. (2010). *Niedermeyer's Electroencephalography: Basic Principles,
540 Clinical Applications, and Related Fields* (Walters Klutter -Lippincott Williams & Wilkins)
- 541 Sellers, E. W., Kübler, A., and Donchin, E. (2006). Brain-computer interface research at the University of
542 South Florida cognitive psychophysiology laboratory: The P300 speller. *IEEE Transactions on Neural
543 Systems and Rehabilitation Engineering* 14, 221–224. doi:10.1109/TNSRE.2006.875580
- 544 Tibon, R. and Levy, D. A. (2015). Striking a balance: analyzing unbalanced event-related potential data.
545 *Frontiers in psychology* 6, 555. doi:10.3389/fpsyg.2015.00555
- 546 Van De Sande, K., Gevers, T., and Snoek, C. (2010). Evaluating color descriptors for object and
547 scene recognition. *IEEE Transactions on Pattern Analysis and Machine Intelligence* 32, 1582–1596.
548 doi:10.1109/TPAMI.2009.154
- 549 Van Drongelen, W. (2006). *Signal processing for neuroscientists: an introduction to the analysis of
550 physiological signals* (Academic press)
- 551 Vedaldi, A. and Fulkerson, B. (2010). VLFeat - An open and portable library of computer vision algorithms.
552 *Design* 3, 1–4. doi:10.1145/1873951.1874249

- 553 Wolpaw, J. and E., W. (2012). *Brain-Computer Interfaces: Principles and Practice* (Oxford University
554 Press)
- 555 Yamaguchi, T., Fujio, M., Inoue, K., and Pfurtscheller, G. (2009). Design method of morphological
556 structural function for pattern recognition of EEG signals during motor imagery and cognition. In *Fourth*
557 *International Conference on Innovative Computing, Information and Control (ICICIC)*. 1558–1561.
558 doi:10.1109/ICICIC.2009.161

5 APPENDIX

559 This section describes the differences between the HIST algorithm described in this work and the SIFT
560 Descriptor (Vedaldi and Fulkerson, 2010).

- 561 • SIFT Detector and custom frame: The SIFT Detector provides the keypoint localization information in
562 the standard SIFT method. The keypoint localization information is stored in a *frame* data structure
563 which is composed of the keypoint center location (x_{kp}, y_{kp}) , patch scale s and patch orientation ϕ :
564 $(x_{kp}, y_{kp}, s, \phi)$. In the HIST proposal the keypoint location and patch parameters are directly specified
565 over the plot image in order to detect the P300 response (see Section 2.2.3). Hence, the SIFT Detector
566 is not being used in this implementation.
- 567 • Patch Scale: Whereas in the standard SIFT implementation the patch is a squared region and there is
568 only one SIFT scale parameter, in HIST a different scale parameter can be assigned to the horizontal
569 and vertical axis. This is a very important modification because otherwise signal plots which extend
570 only on the horizontal direction of the plot image could not be entirely covered. By using a rectangular
571 patch, there isn't any constraint on its size and it can be adjusted by neurophysiological priors to map
572 any expected waveform.
- 573 • Octave Selection: A gradient image is used to obtain the oriented gradients and calculate the histogram
574 of gradient orientations. In SIFT, these gradient images are downsampled and smoothed by a Gaussian
575 filter. The SIFT Descriptor calls *octave* to each downsampling level (Lowe, 2004; Rey-Otero and
576 Delbracio, 2014). The standard SIFT Descriptor estimates the octave to use on the gradient image
577 based on the image size and patch parameters. The HIST method uses only the first octave which
578 means that the gradient image has the same size as the original image, without any downsampling
579 operation.
- 580 • First octave smoothing: Additionally, the SIFT Descriptor performs a smoothing operation by applying
581 a Gaussian filter on the gradient image regardless of the octave. In the HIST method, this operation is
582 not implemented.
- 583 • Patch Orientation: We verified experimentally that the patch orientation ϕ does not provide any extra
584 utility for the extraction of characteristics waveforms from plots. Hence, this patch orientation is fixed
585 to zero (vertical, pointing upwards in Figure 4).
- 586 • Rotations: SIFT was designed to allow affine invariance, i.e. to be robust to rotations and scale
587 modifications of patterns in images. It was not found, so far, of any utility to rotate the patch to capture
588 the signal waveform.
- 589 • Descriptor Gaussian Smoothing: On the standard SIFT Descriptor, a Gaussian smoothing operation is
590 performed on the calculated SIFT descriptor to increase the importance of gradients from pixels closer
591 to the center of the patch. In this case, this is found to be in detriment of the waveform characterization
592 and is not used.

- 593 • SIFT Descriptor Codification: The SIFT descriptor d is a 128-dimension feature vector, as described in
594 Section 2.1.3. Histogram values are double-precision floating point numbers, all positive, and they are
595 accumulated on each coordinate of this vector. Once all the gradients are summarized, the following
596 operations are performed:
597 • The descriptor is ℓ -2 normalized (i.e all the values are divided by the euclidean norm of the
598 descriptor).
599 • Each value is clamped to 0.2. This means that any value above 0.2 is set to 0.2.
600 • The descriptor is ℓ -2 re-normalized again (Rey-Otero and Delbracio, 2014).

601 This generates a 128-vector of double precision floating point numbers, between $[0, 1]$. The HIST
602 implementation was modified to use the cosine distance (Arandjelovic and Zisserman, 2012). Hence
603 the descriptor is rescaled to $[-1, 1]$. Output values are cast to single-precision floating point numbers
604 (i.e. floats). This yields an effective 128-vector of floats between $[-1, 1]$.

Table 1. Character recognition rates for the public dataset of ALS patients using the Histogram of Gradient (HIST) calculated from single-channel plots. Performance rates using single-channel signals with the SVM classifier are shown for comparison. The best performing channel *bpc* for each method is visualized

Participant	<i>bpc</i>	HIST	<i>bpc</i>	Single Channel SVM
1	Cz	35%	Cz	15%
2	Fz	85%	PO8	25%
3	Cz	25%	Fz	5%
4	PO8	55%	Oz	5%
5	PO7	40%	P3	25%
6	PO7	60%	PO8	20%
7	PO8	80%	Fz	30%
8	PO7	95%	PO7	85%

Table 2. Character recognition rates for the own dataset of healthy subjects using the Histogram of Gradient (HIST) calculated from single-channel plots. Performance rates using single-channel signals with the SVM classifier are shown for comparison. The best performing channel *bpc* for each method is visualized.

Participant	<i>bpc</i>	HIST	<i>bpc</i>	Single Channel SVM
1	Oz	40%	Cz	10%
2	PO7	30%	Cz	5%
3	P4	40%	P3	10%
4	P4	45%	P4	35%
5	P4	60%	P3	10%
6	Pz	50%	P4	25%
7	PO7	70%	P3	30%
8	P4	50%	PO7	10%

Table 3. Character recognition rates and the best performing channel *bpc* for the public dataset of ALS patients using the Histogram of Gradient (HIST) (repeated here for comparison purposes). Performance rates obtained by SWLDA and SVM classification algorithms with a multichannel concatenated feature.

Participant	<i>bpc</i> for HIST	HIST	Multichannel SWLDA	Multichannel SVM
1	Cz	35%	45%	40%
2	Fz	85%	30%	50%
3	Cz	25%	65%	55%
4	PO8	55%	40%	50%
5	PO7	40%	35%	45%
6	PO7	60%	35%	70%
7	PO8	80%	60%	35%
8	PO7	95%	90%	95%

Table 4. Character recognition rates and the best performing channel *bpc* for the own dataset of healthy subjects using the Histogram of Gradient (HIST) (repeated here for comparison purposes). Performance rates obtained by SWLDA and SVM classification algorithms with a multichannel concatenated feature.

Participant	<i>bpc</i> for HIST	HIST	Multichannel SWLDA	Multichannel SVM
1	Oz	40%	65%	40%
2	PO7	30%	15%	10%
3	P4	40%	50%	25%
4	P4	45%	40%	20%
5	P4	60%	30%	20%
6	Pz	50%	35%	30%
7	PO7	70%	25%	30%
8	P4	50%	35%	20%

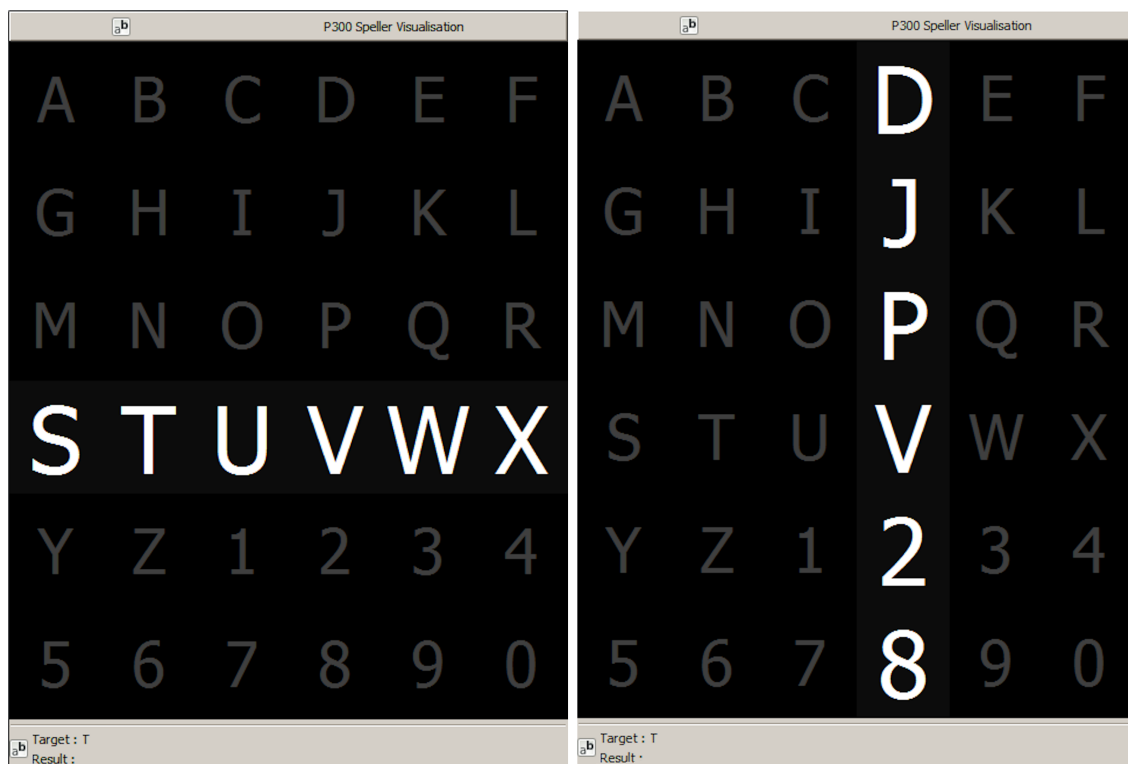


Figure 1. Example of the 6×6 Speller Matrix used in the study obtained from the OpenVibe software. Rows and columns flash in random permutations.

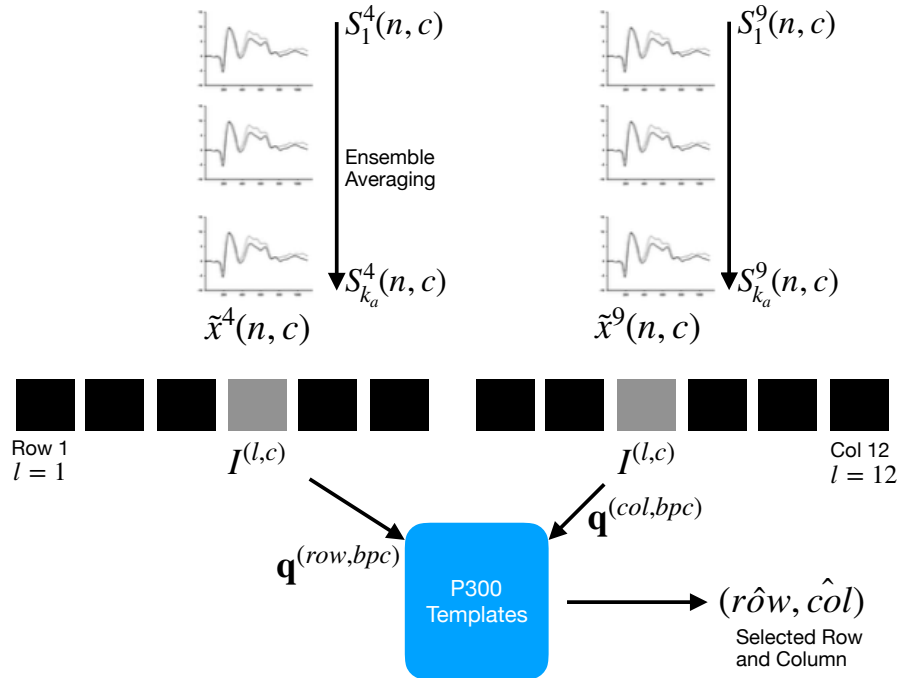


Figure 2. For each column and row, an averaged, standardized and scaled signal $\tilde{x}^l(n, c)$ is obtained from the segments S_i^l corresponding to the k_a intensification sequences with $1 \leq i \leq k_a$ and location l varying between 1 and 12. From the averaged signal, the image $I^{(l,c)}$ of the signal plot is generated and each descriptor is computed. By comparing each descriptor against the set of templates, the P300 ERP can be detected, and finally the desired letter from the matrix can be inferred.

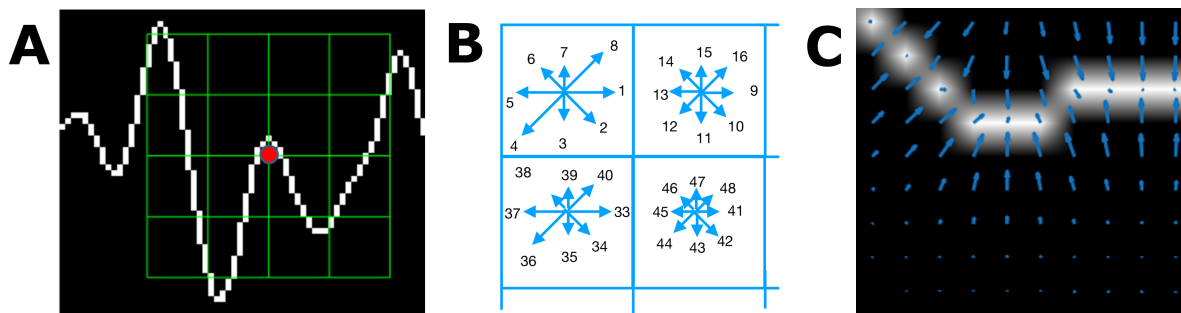


Figure 3. (A) Example of a plot of the signal, a keypoint and the corresponding patch. (B) A scheme of the orientation's histogram computation. Only the upper-left four blocks are visible. The first eight orientations of the first block, are labeled from 1 to 8 clockwise. The orientation of the second block $B_{1,2}$ is labeled from 9 to 16. This labeling continues left-to-right, up-down until the eight orientations for all the sixteen blocks are assigned. They form the corresponding descriptor of 128 coordinates. The length of each arrow represent the value of the histogram on each direction for each block. (C) Vector field of oriented gradients. Each pixel is assigned an orientation and magnitude calculated using finite differences.

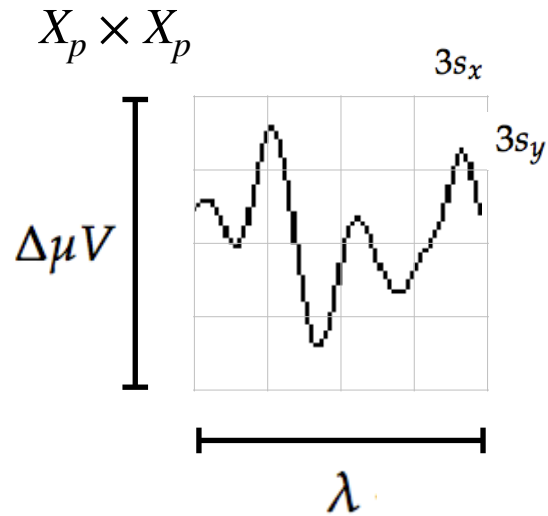


Figure 4. The scale of local patch is selected in order to capture the whole transient event. The size of the patch is $X_p \times X_p$ pixels. The vertical size consists of 4 blocks of size $3s_y$ pixels which is high enough as to contain the signal $\Delta\mu V$, the peak-to-peak amplitude of the transient event. The horizontal size includes 4 blocks of $3s_x$ and covers the entire duration in seconds of the transient signal event, λ .

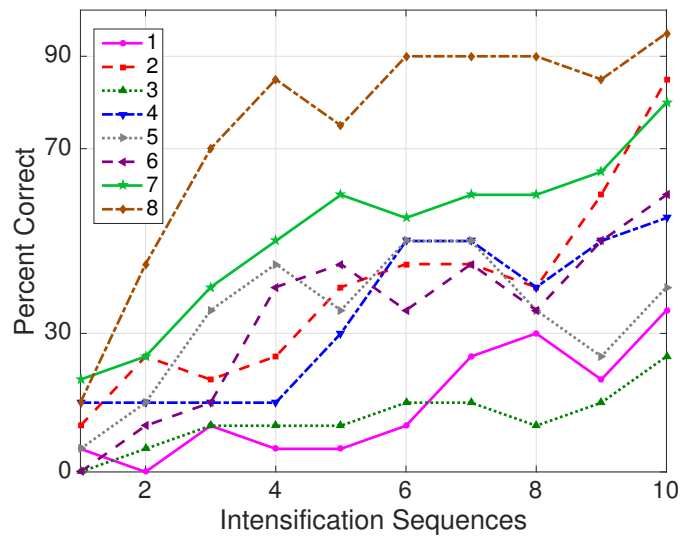


Figure 5. Performance curves for the eight subjects included in the dataset of ALS patients. Three out of eight subjects achieved the necessary performance to implement a valid P300 speller.

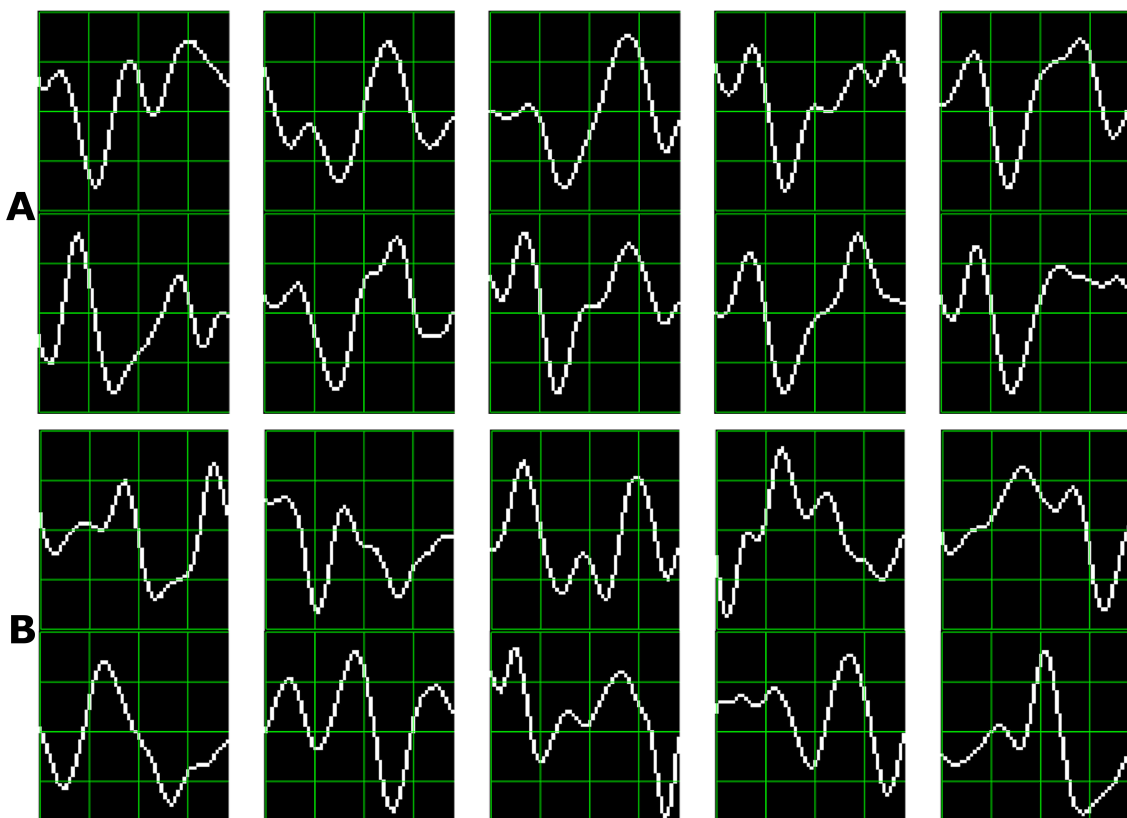


Figure 6. Ten sample P300 template patches for subjects 8 (A) and 3 (B) of the ALS Dataset. Downward deflection is positive polarity.